Letter

Edge density of bulk states due to relativity

Matthew D. Horner* and Jiannis K. Pachos
School of Physics and Astronomy, University of Leeds, Leeds LS2 9JT, United Kingdom

(Received 17 May 2021; revised 7 July 2021; accepted 28 July 2021; published 10 August 2021)

The boundaries of quantum materials can host a variety of exotic effects such as topologically robust edge states or anyonic quasiparticles. Here, we show that fermionic systems such as graphene that admit a low-energy Dirac description can exhibit counterintuitive relativistic effects at their boundaries. As an example, we consider carbon nanotubes and demonstrate that relativistic bulk spinor states can have nonzero charge density on the boundaries, in contrast to the sinusoidal distribution of nonrelativistic wave functions that are necessarily zero at the boundaries. This unusual property of relativistic spinors is complementary to the linear energy dispersion relation exhibited by Dirac materials and can influence their coupling to leads, transport properties, or their response to external fields.

DOI: 10.1103/PhysRevB.104.L081402

Introduction. Several materials have low-energy quantum properties that are faithfully described by the relativistic Dirac equation. The celebrated example of graphene owes some of its unique properties, such as the half-integer quantum Hall effect [1–3] and the Klein paradox effect [4,5], to the relativistic linear dispersion relation describing its low-energy sector. This is by no means a singular case. A wide range of materials have been recently identified that admit one-, two-, or three-dimensional (1D, 2D, or 3D) relativistic Dirac descriptions, including many topological insulators and d-wave superconductors [6–11]. The unusual dispersion relation of Dirac materials gives rise to effective spinors, where the sublattice degree of freedom is encoded in the pseudospin components. Nevertheless, the emerging excitations are spinor quasiparticles that can exhibit novel transport properties or responses to external fields akin only to relativistic physics [5].

Here, we present another counterintuitive aspect of relativistic physics in Dirac materials manifested by the behavior of bulk states at the boundaries. In general, the choice of boundary conditions one imposes on single-particle wave functions of a system must ensure its Hamiltonian remains Hermitian. For the example of a nonrelativistic particle in a box obeying the Schrödinger equation, the boundary conditions are simply that the wave function vanishes on the walls of the box. However, for spin-1/2 particles of mass m obeying the $(2+1)$D Dirac equation

$$(-i\alpha^i\partial_i+\beta m)\psi(\boldsymbol{r})=E\psi(\boldsymbol{r}),\quad \psi(\boldsymbol{r})=\begin{pmatrix}\psi_\uparrow(\boldsymbol{r})\\ \psi_\downarrow(\boldsymbol{r})\end{pmatrix},\qquad (1)$$

where α^i and β are the 2×2 Dirac alpha and beta matrices, vanishing of the spinor $\psi(\boldsymbol{r})$ is not possible on all boundaries without the solution being trivially zero everywhere. The requirement that the Dirac Hamiltonian $h=-i\alpha^i\partial_i+\beta m$ is Hermitian with respect to the inner product $\int_D d^2r\psi^\dagger(\boldsymbol{r})\phi(\boldsymbol{r})$ on a finite domain D is that the charge current $J^i(\boldsymbol{r})=\psi^\dagger(\boldsymbol{r})\alpha^i\psi(\boldsymbol{r})$ normal to the boundary ∂D is zero for all spinors. In other words, if $\hat{\boldsymbol{n}}$ is the outward pointing normal to the boundary, then

$$\hat{\boldsymbol{n}}(\boldsymbol{r}_0)\cdot\boldsymbol{J}(\boldsymbol{r}_0)=0 \qquad (2)$$

for all points $\boldsymbol{r}_0\in\partial D$ [12]. This condition ensures that particles are trapped in D. In contrast to the nonrelativistic case, the zero flux condition of Eq. (2) allows for bulk solutions $\psi(\boldsymbol{r})$ whose charge density $\rho(\boldsymbol{r}_0)=\psi^\dagger(\boldsymbol{r}_0)\psi(\boldsymbol{r}_0)$ is nonzero on the boundaries [13,14].

To exemplify our investigation, we consider how bulk spinor states behave at the edges of a zigzag carbon nanotube—a system which is described by the Dirac equation of Eq. (1). We find that bulk states have support on the edges of the nanotube depending on the size of the system. Importantly, these relativistic effects become more dominant for gapless nanotubes, corresponding to systems with a multiple of three unit cells in circumference, or when the length of the nanotube is small. Such relativistic properties of spinor eigenstates are expected to be present in all Dirac-like materials and are complementary to the typically linear dispersion relation they exhibit. Bulk states with nonzero density at the boundaries are expected to impact the coupling of Dirac materials to external leads, their transport properties, or their response to external magnetic fields.

Relativistic description of zigzag carbon nanotubes. The honeycomb lattice of graphene is formed from two triangular sublattices A and B. We take the two basis vectors $\boldsymbol{n}_x,\boldsymbol{n}_y$ and we take the vertical links as our unit cells, as shown in Fig. 1. We label our lattice sites with the pair $(\boldsymbol{r},\mu)$, where $\boldsymbol{r}=x\boldsymbol{n}_x+y\boldsymbol{n}_y$ labels the position of the unit cell with non-Cartesian coordinates $x,y\in\mathbb{Z}$, while $\mu\in\{A,B\}$ labels the site within the unit cell. The Hamiltonian of the system is given by $H=-t\sum_{\langle\boldsymbol{r},\boldsymbol{r}'\rangle}a^\dagger_{\boldsymbol{r}}b_{\boldsymbol{r}'}+\text{H.c.}$, where $a^\dagger_{\boldsymbol{r}}$ ($b^\dagger_{\boldsymbol{r}}$) creates a fermion on sublattice A (B) of unit cell $\boldsymbol{r}$ [5]. Bloch momenta are given by $\boldsymbol{k}=\frac{1}{2\pi}(k_x\boldsymbol{G}_x+k_y\boldsymbol{G}_y)$, where $\boldsymbol{G}_x,\boldsymbol{G}_y$

*py13mh@leeds.ac.uk

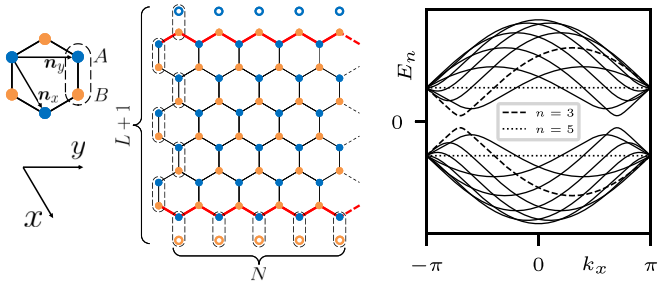

FIG. 1. Left: The honeycomb lattice comprising two triangular sublattices A and B. The lattice basis vectors $\boldsymbol{n}_x = \frac{1}{2}(1, -\sqrt{3})$ and $\boldsymbol{n}_y = (1, 0)$ are depicted with corresponding non-Cartesian coordinates x and y. A nanotube with zigzag boundaries (red lines) is depicted with length L corresponding to $L + 1$ unit cells (dashed ovals) in the $\boldsymbol{n}_x$ direction while the $\boldsymbol{n}_y$ direction is periodic with circumference N. The boundary condition is given by the top A sites and bottom B sites having zero population. Right: The band structure of a zigzag nanotube of circumference $N = 10$ is displayed, where $n = 3$ (dashed lines) is one of the two minimum gap bands. All bands have a single minimum except $n = N/2 = 5$ which is completely flat (dotted line).

are the reciprocal basis vectors and $k_x, k_y \in [-\pi, \pi]$ are the corresponding coordinates of the Brillouin zone (BZ) (see Appendix A of the Supplemental Material [15]).

To study the low-energy properties of a finite zigzag nanotube, we first take the continuum and thermodynamic limit in the $\boldsymbol{n}_x$ direction only, while keeping the periodic $\boldsymbol{n}_y$ direction finite and discrete, with N unit cells in circumference. This gives rise to N bands parametrized by momenta $k_y = 2n\pi/N$, where n is an integer [16,17]. The nth band has the one-dimensional dispersion relation

$$E_n(k_x) = \pm t\sqrt{3 + 2g_n(k_x)}, \tag{3}$$

where $g_n(k_x) = \cos(\frac{2n\pi}{N}) + \cos(\frac{2n\pi}{N} - k_x) + \cos(k_x)$. The zigzag nanotube is typically gapped, unlike an infinite flat sheet of graphene which is gapless. Each conduction band contains a single minima, as seen in Fig. 1, which dictates the low-energy physics for that particular band. Our model is a simplified version of a carbon nanotube as we ignore effects due to curvature and spin-orbit coupling that are not relevant to our investigation [5,17–22].

Following the literature [20,22], we expand the Hamiltonian about the minima of Eq. (3) by letting $k_x = K_{\min} + p$, for each band n, yielding the $(1 + 1)$D massive Dirac Hamiltonian $H_n = \int dx \psi_n^\dagger h_n \psi_n$, with

$$h_n = -ie_n\sigma^y\partial_x + \Delta_n\sigma^x, \quad \psi_n(x) = \begin{pmatrix} a_n(x) \\ b_n(x) \end{pmatrix}, \tag{4}$$

where the sublattices A and B of the unit cell are encoded on the pseudospin components, $e_n = 2t\cos(\frac{n\pi}{N})$ is the spatial component of the zweibein, and Δ_n is the energy gap of the nth band, given by

$$\Delta_n = t\left[2\cos\left(\frac{n\pi}{N}\right) - 1\right]. \tag{5}$$

See Appendix A of the Supplemental Material for a derivation [15]. We now truncate the length of the nanotube to a finite length L. We construct standing waves $\psi(x) = [\psi_A(x), \psi_B(x)]^{\mathrm{T}}$ from forward and backward propagating eigenstates of h_n of Eq. (4). The zigzag boundary conditions are $\psi_A(0) = \psi_B(L) = 0$, where $x = 0$ and $x = L$ are the coordinates of the unit cells of the top and bottom boundaries, as shown in Fig. 1 [20,21]. These conditions obey the zero flux condition of Eq. (2). This gives the solutions

$$\psi_{n,p}(x) = \mathcal{N}_{n,p}\begin{pmatrix} \sin(px) \\ \sin(px + \theta_{n,p}) \end{pmatrix}, \tag{6a}$$

$$\theta_{n,p} = \arg(\Delta_n + ie_n p), \tag{6b}$$

where $\mathcal{N}_{n,p}$ is a normalization constant and $\theta_{n,p}$ is a relative phase shift between the A and B sublattice wave functions. The quantized momenta p are solutions to the transcendental equation

$$pL + \theta_{n,p} = m\pi, \quad m \in \mathbb{N}, \tag{7}$$

which can be solved numerically (see Appendix A of the Supplemental Material [15]). Note that the wave functions of Eq. (6a) correspond to bulk states, however, graphene with zigzag boundaries also supports zero-energy states localized at the edges [11]. Edge states correspond to complex solutions of Eq. (7) and are not considered here [5,20,21].

Relativistic edge effects of bulk states. The $U(1)$ electric charge density of $(1 + 1)$D Dirac spinors $\psi = (\psi_A, \psi_B)^T$ is given by $\rho = \psi^\dagger\psi = |\psi_A|^2 + |\psi_B|^2$. With our interpretation of the pseudospin components $\psi_A(x)$ and $\psi_B(x)$ as the sublattice wave functions, where x labels the unit cell, ρ is therefore the charge density with respect to the unit cells. For the bulk standing wave solutions of Eq. (6a), we have

$$\rho_{n,p}(x) = |\mathcal{N}_{n,p}|^2[\sin^2(px) + \sin^2(px + \theta_{n,p})], \tag{8}$$

which gives a charge density at the boundaries of

$$\rho_{n,p}(0) = \rho_{n,p}(L) = |\mathcal{N}_{n,p}|^2\sin^2(\theta_{n,p}). \tag{9}$$

We see that it is possible to have $\rho_{n,p}(0) \neq 0$ due to the phase difference $\theta_{n,p}$, which is purely a relativistic effect.

The edge charge density of bulk states is maximal when $\theta_{n,p} = \pm\pi/2$. Referring to Eq. (6b), this is achieved when $\Delta_n = 0$, i.e., when the nth band is gapless. From Eq. (5) we see that the gap closes if $n/N = \pm 1/3$ which is only possible if N is a multiple of three. Note that, for a gapless band, the charge density of Eq. (8) is also completely uniform with

$$\rho_{n,p}(x) = \frac{1}{L}, \tag{10}$$

which is independent of the momentum p, where we have chosen a 1D normalization. On the other hand, when the system is gapped, then the density oscillates along the length of the nanotube and becomes vanishingly small at the edges. This shift in behavior of the charge density reflects the expected transition from the relativistic to nonrelativistic regime witnessed in confined Dirac particles as their mass increases [13].

The stark contrast between gapped and gapless systems is confirmed numerically (see Appendix B of the Supplemental Material for numerical details [15]). The left-hand column of Fig. 2 shows the edge density ρ of the ground state of a system of length $L = 200$ for varying circumferences N. When N is a multiple of three, i.e., when the system is gapless, the

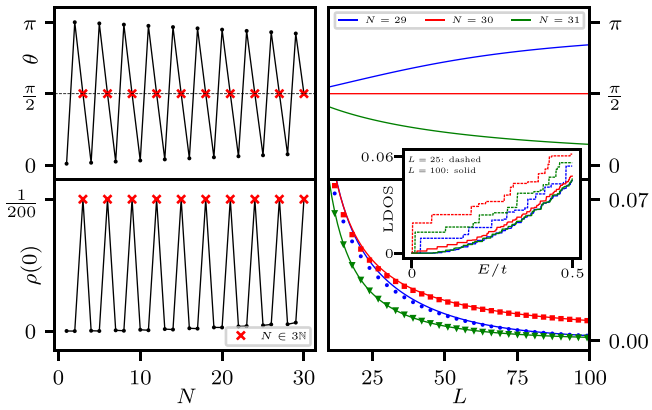

FIG. 2. Left: The phase shifts $\theta \equiv \theta_{n,p}$ of Eq. (6b) and the numerically measured edge densities $\rho(0) \equiv \rho_{n,p}(0)$ vs circumference N for the ground state of a system of fixed length $L = 200$. When N is a multiple of three, i.e., when the system is gapless, the phase shift is $\theta = \pi/2$ and the edge density is $\rho(0) = 1/L = 0.005$, confirming Eq. (10). Right: The phase shifts θ and edge densities $\rho(0)$ vs system length L for the ground state of the gapless systems $N = 30$ and its two neighboring gapped systems $N = 29$ and $N = 31$. The solid line represents the analytical formulas while the points represent numerics. The edge density for the gapless system $N = 30$ goes as $1/L$, while for gapped systems $N = 29$ and $N = 31$ the edge density tends to zero quickly, in agreement with Eq. (9). Inset: The integrated LDOS at the edge $x = 0$ for a nanotube of circumferences $N = 29, 30, 31$ and lengths $L = 25$ (dashed lines) and $L = 100$ (solid lines). The LDOS displays the predicted behavior of maximizing for gapless systems ($N = 30$) and increasing with smaller system size L.

edge density spikes to the expected value of $1/L = 0.005$. On the other hand, when N is not a multiple of three, i.e., when the system is gapped, the edge density is small. This behavior is a consequence of the highly oscillating phase shift θ. When N is a multiple of three, the phase shift is $\pi/2$ exactly, maximizing the edge density according to Eq. (9). The smaller N is, the stronger the effect as the difference between gapped and gapless systems is much stronger due to the gaps being larger. However, as N increases, all zigzag nanotubes tend towards gapless systems even if N is not a multiple of three, as there exists a band n such that $n/N \approx \pm 1/3$ when N is large, so the gap of Eq. (5) begins to close, so all systems begin to behave similarly.

The relativistic boundary effects also have a system length dependence [13]. The right-hand column of Fig. 2 shows the numerically measured edge density ρ of the ground state of a gapless system $N = 30$ and its two neighboring gapped systems $N = 29$ and $N = 31$ for varying system lengths L. The edge density of the gapless system $N = 30$ goes as $1/L$ whereas the edge density gapped systems $N = 29$ and $N = 31$ tend to zero quickly, both in accordance with Eq. (9). It is worth noting that, despite the fact that the analytic results have been derived in the large L limit where the continuum approximation holds, the numerics and analytics are in surprisingly good agreement even for very small L. This verifies the theoretically predicted relativistic effects of nanotubes with small length L where the violation of the nonrelativistic zero edge density is expected. Note that this behavior repeats itself for any N that is a multiple of three and its two neighboring sizes above and below, which the left-hand side of Fig. 2 demonstrates.

To explain the system size dependence of the charge density, note that for very small L the allowed momenta p satisfying Eq. (7) become very large. In this case, the imaginary contribution to the phase $\theta_{n,p} = \arg(\Delta_n + ie_n p)$ dominates, giving $\theta_{n,p} \approx \pi/2$ even if the gap is nonzero, as seen in the right-hand column of Fig. 2. Hence, the edge density of Eq. (9) becomes significant for small system sizes. For the gapless case, the phase is exactly equal to $\pi/2$ regardless of the value of p or system size L. This yields a uniform charge density throughout the nanotube, resulting in the $1/L$ edge density as observed.

Finally, Fig. 2 shows the integrated local density of states (LDOS) on the edge at $x = 0$ given by $N(E, \boldsymbol{r}) = \sum_m \rho_m(\boldsymbol{r})\Theta(E - E_m)$, where $\rho_m(\boldsymbol{r})$ is the unit cell charge density of the mth eigenstate of the 2D model with eigenvalue E_m. We present this for systems $N = 29, 30, 31$ and $L = 25, 100$. The edge LDOS is maximized for a fixed L when the system is gapless, so for $N = 30$ in this case. Moreover, the LDOS increases as the system size decreases, which provides a clear signature for the observation of the relativistic edge effect.

To summarize, the edge density is prominent if either the system is gapless, so N is a multiple of three, or the system length L is small. The typical lattice constant of a nanotube is given by $|\boldsymbol{n}_x| = |\boldsymbol{n}_y| \approx 2.46$ Å [17,23], so Fig. 2 applies to systems on the order of 1 nm in diameter and 10 nm in length. However, the dependence on whether or not the system is gapless is very strong, so this effect holds for much larger circumferences N and lengths L. Therefore, we expect these results to hold for a wide range of experimentally accessible sizes.

Relativistic spinors from nonrelativistic wave functions. To explain the emergence of relativistic boundary effects from a nonrelativistic model, we focus on the sublattice wave functions ψ_A and ψ_B. For concreteness, we examine a nanotube of dimension $(N, L) = (30, 200)$ and $(N, L) = (31, 200)$ which have gapless and gapped spectra, respectively.

In the left-hand column of Fig. 3 we compare the numerical sublattice wave functions $\psi_A(x)$, $\psi_B(x)$ and the charge densities $\rho(x)$ to the analytical results of Eqs. (6a) and (8), respectively, for the first three excited states above the Fermi energy for the gapless system $(N, L) = (30, 200)$. We see that the sublattice wave functions ψ_A and ψ_B are highly out of phase and maximize the edge support at $x = L$ and $x = 0$, respectively, yielding a charge density $\rho(x)$ with minor oscillations about the predicted uniform value of $1/L = 0.005$. These oscillations are caused by finite-size effects.

In the right-hand column of Fig. 3, we present the same information for the gapped system $(N, L) = (31, 200)$. Despite N increasing only by 1, the fact the system now has a gap results in wave functions $\psi_A(x)$ and $\psi_B(x)$ that contrast considerably to the gapless case, with a charge density $\rho(x)$ that displays a more Schrödinger-like oscillatory profile. As the system size L increases, the relative phase shift θ modulo π between $\psi_A(x)$ and $\psi_B(x)$ decreases, as seen in Fig. 2, and the wave functions begin to display the Schrödinger-like profile that tends to zero on the boundaries. However, this is not the case for gapless systems as the phase shift is always $\pi/2$ regardless of system size, as seen in Fig. 2.

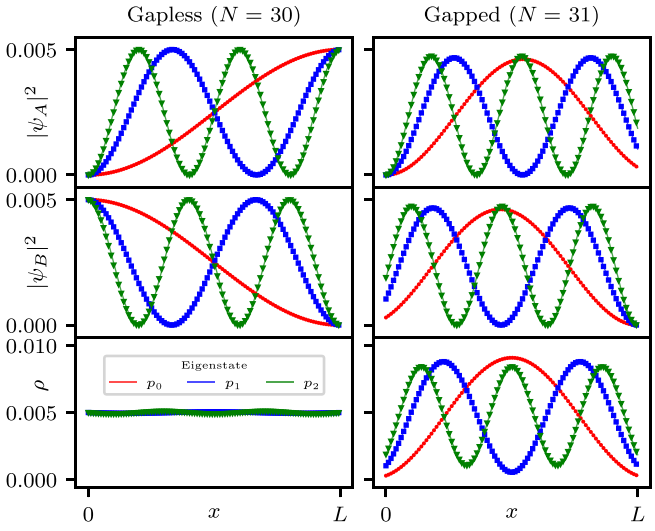

FIG. 3. Left: A comparison of the analytical wave functions $|\psi_A|^2$ and $|\psi_B|^2$ of Eq. (6a) and charge densities ρ of Eq. (9) to the numerical simulation (markers) for the gapless system $(N, L) = (30, 200)$. We present the first three excited states above the Fermi energy $E = 0$. We observe the wave functions act highly relativistically, with a large boundary support and uniform charge density of $1/L = 0.005$. Right: We present the same information for the gapped system $(N, L) = (31, 200)$. The behavior contrasts highly with the gapless system despite N only being greater by one. The wave functions and densities display a Schrödinger-like profile with a much smaller edge density that tends to zero as L increases as seen in Fig. 2.

We now analyze the total wave functions Ψ_j of the lattice fermions, where $j \in \mathbb{N}$ is the real space coordinate of the bipartite lattice, alternating between sublattices A and B. This coordinate should be contrasted to the unit cell coordinate x of the spinor $\psi(x)$. Figure 4 shows the wave functions of the single-particle eigenstate with the most negative energy below the Fermi energy, $\Psi_{0,j}$, and the first single-particle eigenstate above the Fermi energy, Ψ_j, for a system of dimension $(N, L) = (30, 9)$.

The wave functions $\Psi_{0,j}$ and Ψ_j are both nonrelativistic wave functions which vanish on the boundaries. This is to be expected as the microscopic model is nonrelativistic. However, due to high-frequency oscillations, the support of Ψ_j on each sublattice is highly out of phase. Comparing with the left-hand column of Fig. 3, we see that these oscillations give the impression of two separate wave functions faithfully described by the components of a Dirac spinor. Nonrelativistically, we expect the system to behave as a particle in a box, so we take the ansatz wave function $\Psi_j \propto \sin(pj)$. From inspection, we see that this matches the numerics for momenta $p = (l + 1)\pi/2l$, where $l = 2L + 1$ is the total length of the bipartite chain and $L + 1$ is the number of unit cells as defined in Fig. 1. This gives a wavelength comparable to the lattice spacing. Therefore, the emergent relativistic physics described by the spinor of Eq. (6a) is a consequence of aliasing from sampling a high-frequency nonrelativistic wave function at

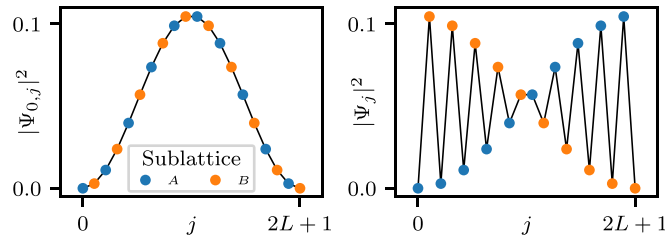

FIG. 4. The full single-particle ground state $\Psi_{0,j}$ and the first state above the Fermi energy Ψ_j for a system of size $(N, L) = (30, 9)$. The emergent relativistic physics near the Fermi energy can be seen clearly as a result of aliasing of a high-frequency Schrödinger wave function. Comparing this with the left-hand column of Fig. 3, we see how the sublattice wave functions ψ_A and ψ_B described by the spinor Eq. (6a) emerge.

discrete intervals. This effect is independent of length L. Such high-frequency wave functions correspond to the middle of the spectrum where the relativistic linear dispersion is present.

On the other hand, gapped systems display a Schrödinger-like wave function for both $\Psi_{0,j}$ and Ψ_j if the system length L is large. This can be seen clearly in the right-hand column of Fig. 3 where the sublattice wave functions are almost in phase. The total wave functions that describe these can also be described by the ansatz wave function of a particle in a box, but for a small p instead, so A and B sublattices are now more in phase, similar to the left-hand side of Fig. 4. We also see this in the right-hand side of Fig. 2 where the edge densities drop to zero on the walls, suggesting a nonrelativistic behavior.

Conclusion. Our analysis demonstrates that relativistic effects can dominate certain geometries of Dirac materials, resulting in large edge support. We studied this effect analytically and numerically for zigzag carbon nanotubes and demonstrated that it holds strongly for a wide range of experimentally accessible sizes. We found that the effect is dominant when the system is either gapless or has a small length on the order of 10 nm. Nevertheless, this relativistic effect is general and it is expected to be present in 1D, 2D, and 3D materials with the same qualitative properties presented here. While high edge densities of bulk states should be measurable with scanning tunneling microscopy (STM) [24–27], it is expected to have a significant effect on the conductivity of the material when attaching leads to its boundaries or its response to a magnetic field [20,21,28,29]. In addition, determining if such effects will be present in 2D materials containing a finite density of defects which effectively imposes boundary conditions on the wave functions within the material will be intriguing [5,30–32]. We leave these questions for a future work.

Acknowledgments. In compliance with EPSRC policy framework on research data, this publication is theoretical work that does not require supporting research data.

We would like to thank Oscar Cespedes, Jamie Lake, Alex Little, and Satoshi Sasaki for inspiring conversations. This work was supported by the EPSRC Grant No. EP/R020612/1.

[1] K. S. Novoselov, A. K. Geim, S. V. Morozov, D. Jiang, M. I. Katsnelson, I. V. Grigorieva, S. V. Dubonos, and A. A. Firsov, Two-dimensional gas of massless Dirac fermions in graphene, Nature (London) **438**, 197 (2005).

[2] K. S. Novoselov, Z. Jiang, Y. Zhang, S. V. Morozov, H. L. Stormer, U. Zeitler, J. C. Maan, G. S. Boebinger, P. Kim, and A. K. Geim, Room-temperature quantum Hall effect in graphene, Science **315**, 1379 (2007).

[3] S. Fujita and A. Suzuki, Theory of the half-integer quantum Hall effect in graphene, Int. J. Theor. Phys. **55**, 4830 (2016).

[4] M. I. Katsnelson, K. S. Novoselov, and A. K. Geim, Chiral tunnelling and the Klein paradox in graphene, Nat. Phys. **2**, 620 (2006).

[5] A. H. Castro Neto, F. Guinea, N. M. R. Peres, K. S. Novoselov, and A. K. Geim, The electronic properties of graphene, Rev. Mod. Phys. **81**, 109 (2009).

[6] T. Wehling, A. Black-Schaffer, and A. Balatsky, Dirac materials, Adv. Phys. **63**, 1 (2014).

[7] J. E. Moore, The birth of topological insulators, Nature (London) **464**, 194 (2010).

[8] S. Jia, S.-Y. Xu, and M. Z. Hasan, Weyl semimetals, Fermi arcs and chiral anomalies, Nat. Mater. **15**, 1140 (2016).

[9] M. Z. Hasan and C. L. Kane, Colloquium: Topological insulators, Rev. Mod. Phys. **82**, 3045 (2010).

[10] M. Z. Hasan and J. E. Moore, Three-dimensional topological insulators, Annu. Rev. Condens. Matter Phys. **2**, 55 (2011).

[11] B. A. Bernevig and T. L. Hughes, *Topological Insulators and Topological Superconductors* (Princeton University Press, Princeton, NJ, 2013), pp. 80–90.

[12] M. V. Berry and R. Mondragon, Neutrino billiards: time-reversal symmetry-breaking without magnetic fields, Proc. R. Soc. London, Ser. A **412**, 53 (1987).

[13] P. Alberto, C. Fiolhais, and V. M. S. Gil, Relativistic particle in a box, Eur. J. Phys. **17**, 19 (1996).

[14] V. Alonso, S. D. Vincenzo, and L. Mondino, On the boundary conditions for the Dirac equation, Eur. J. Phys. **18**, 315 (1997).

[15] See Supplemental Material at http://link.aps.org/supplemental/10.1103/PhysRevB.104.L081402 for detailed calculations of all results and information on numerical methods used.

[16] J.-C. Charlier, X. Blase, and S. Roche, Electronic and transport properties of nanotubes, Rev. Mod. Phys. **79**, 677 (2007).

[17] R. Saito, G. Dresselhaus, and M. S. Dresselhaus, *Physical Properties of Carbon Nanotubes* (Imperial College Press, London, 1998).

[18] C. L. Kane and E. J. Mele, Size, Shape, and Low Energy Electronic Structure of Carbon Nanotubes, Phys. Rev. Lett. **78**, 1932 (1997).

[19] T. Ando, Spin-orbit interaction in carbon nanotubes, J. Phys. Soc. Jpn. **69**, 1757 (2000).

[20] M. Margańska, D. R. Schmid, A. Dirnaichner, P. L. Stiller, C. Strunk, M. Grifoni, and A. K. Hüttel, Shaping Electron Wave Functions in a Carbon Nanotube with a Parallel Magnetic Field, Phys. Rev. Lett. **122**, 086802 (2019).

[21] M. Margańska, M. del Valle, S. H. Jhang, C. Strunk, and M. Grifoni, Localization induced by magnetic fields in carbon nanotubes, Phys. Rev. B **83**, 193407 (2011).

[22] A. R. Akhmerov and C. W. J. Beenakker, Boundary conditions for Dirac fermions on a terminated honeycomb lattice, Phys. Rev. B **77**, 085423 (2008).

[23] A. Altland and B. D. Simons, *Condensed Matter Field Theory* (Cambridge University Press, Cambridge, UK, 2010), pp. 55–58.

[24] E. Y. Andrei, G. Li, and X. Du, Electronic properties of graphene: a perspective from scanning tunneling microscopy and magnetotransport, Rep. Prog. Phys. **75**, 056501 (2012).

[25] P. Kim, T. W. Odom, J. Huang, and C. M. Lieber, Stm study of single-walled carbon nanotubes, Carbon **38**, 1741 (2000).

[26] L. C. Venema, V. Meunier, P. Lambin, and C. Dekker, Atomic structure of carbon nanotubes from scanning tunneling microscopy, Phys. Rev. B **61**, 2991 (2000).

[27] A. Hassanien, M. Tokumoto, Y. Kumazawa, H. Kataura, Y. Maniwa, S. Suzuki, and Y. Achiba, Atomic structure and electronic properties of single-wall carbon nanotubes probed by scanning tunneling microscope at room temperature, Appl. Phys. Lett. **73**, 3839 (1998).

[28] E. A. Laird, F. Kuemmeth, G. A. Steele, K. Grove-Rasmussen, J. Nygård, K. Flensberg, and L. P. Kouwenhoven, Quantum transport in carbon nanotubes, Rev. Mod. Phys. **87**, 703 (2015).

[29] H. Ajiki and T. Ando, Electronic states of carbon nanotubes, J. Phys. Soc. Jpn. **62**, 1255 (1993).

[30] L. A. Algharagholy, Defects in carbon nanotubes and their impact on the electronic transport properties, J. Electron. Mater. **48**, 2301 (2019).

[31] P. T. Araujo, M. Terrones, and M. S. Dresselhaus, Defects and impurities in graphene-like materials, Mater. Today **15**, 98 (2012).

[32] C. Dutreix, H. González-Herrero, I. Brihuega, M. I. Katsnelson, C. Chapelier, and V. T. Renard, Measuring the Berry phase of graphene from wavefront dislocations in Friedel oscillations, Nature (London) **574**, 219 (2019).